Characterization and application of alkanethiolate self-assembled monolayers on Au-coated chips for Ir(IV) and Rh(III) sorption

Vira Zakusilova, Evgeny Tereshatov, Maria Boltoeva, Charles Folden Iii

Characterization and Application of Alkanethiolate Self-Assembled Monolayers on Au-Coated Chips for Ir(IV) and Rh(III) Sorption

Vira Zakusilova[1,2], Evgeny E. Tereshatov[2*], Maria Boltoeva[1], Charles M. Folden III[2,3]

[1] *Université de Strasbourg, CNRS, IPHC, UMR 7178, F-67000 Strasbourg, France*

[2] *Cyclotron Institute, Texas A&M University, College Station, TX 77843, USA*

[3] *Department of Chemistry, Texas A&M University, College Station, TX 77843, USA*

[*] Corresponding author

E-mail addresses: vera.zakusilova@gmail.com; maria.boltoeva@iphc.cnrs.fr;

etereshatov@tamu.edu; Folden@comp.tamu.edu

Abstract

Au-coated Si alpha-particle detectors have been widely used during the chemical characterization of superheavy elements that have been an area of great interest to scientists for decades. Further experiments are aimed at the functionalization of this type of detector to study the chemical properties of meitnerium. It is expected to be a member of the Group 9 elements of the periodic table, and its chemical properties have not been studied before. In this study, self-assembled monolayers (SAMs) of 1-(11-mercaptoundecyl)imidazole (Im-C_{11}-SH) and 12-mercaptododecanoic acid (MDDA) on 1×1 cm^2 Au-coated Si and glass chips were prepared and characterized using several analytical and optical techniques: atomic force microscopy (AFM), nanoprojectile secondary ion mass spectrometry (NP-SIMS), X-ray photoelectron spectroscopy (XPS), ellipsometry, and instrumental neutron activation analysis (INAA). The coverage of Au-coated Si chips with Im-C_{11}-SH SAMs was (99 ± 6)%. NP-SIMS showed quantitative sorption of Rh(III) from an HCl medium, the coverage of Im-C_{11}-SH SAMs with Rh(III) was (81.3 ± 3.8)%.

INAA showed quantitative sorption of Ir(IV) and illustrated that it can be adsorbed from a 5.4 μM initial Ir(IV) solution in 0.55 M HCl on the Im-C_{11}-SH and MDDA SAMs with a surface saturation of (77 ± 12)% and (84 ± 16)%, respectively.

Keywords: Thiolate Self-Assembled Monolayers, 1-(11-mercaptoundecyl)imidazole, 12-mercaptododecanoic acid, Au-Coated Surfaces, Ir(IV) and Rh(III) Sorption

1. Introduction

In the field of studying the chemical properties of superheavy elements ($Z \geq 104$), there is a tradition of coating silicon detectors with Au. One of the first attempts to test such detectors was made during the chemical characterization of element 112, Cn, for which better chemical sorption was observed on modified surfaces rather than non-modified ones [1, 2]. However, element 113, Nh, showed an enhanced reactivity towards Au, preventing the proper chemical characterization of this element [3, 4]. A need for new chemically modified Au-coated Si detectors that will selectively bind the atoms of interest, but with weaker interactions, has emerged. The chemical modification of a pure silicon surface without any metal coating is a much more challenging task, requiring sophisticated moisture-sensitive organic synthesis as well as harsh chemical conditions to break Si-O-Si bridges [5], and this approach does not work well for very sensitive silicon detectors [6]. The superheavy element community is interested in studying the chemical properties of meitnerium (Mt, Z = 109), which have not been characterized yet. This requires the development of corresponding chemical procedures aimed at its two closest expected homologs, Ir and Rh.

A well-known approach to the functionalization of metals, metal oxides, and semiconductors is the formation of self-assembled monolayers (SAMs) on top of them [7-12]. SAMs are arrangements of molecules that can be spontaneously adsorbed on solid surfaces from

a solution or a vapor phase [8]. They are very thin organic layers that are ideally composed of a single monolayer [13]. In general, their thickness is in the order of 1-2 nm and not more than 10 nm [13-16]. SAMs molecules can be divided into three parts: a headgroup, a hydrocarbon chain, and a functional terminal group [8]. Different headgroups can bind to specific metals, metal oxides, and semiconductors [9-12, 17-39].

Alkanethiolate SAMs on the surfaces of noble and coinage metals (Au, Si, Cu, Pd, Pt, and Ni) are the most broadly studied and popular class of SAMs [7-12]. Among all listed metals, there is a preference for Au, and in particular, Au(111). Due to the fact that face-centered cubic metals with a (111) orientation have the lowest surface free energy, such metal surfaces are more stable compared to those with a (100) orientation which undergo massive reconstructions [40, 41]. Au is the most widely used metal during the SAMs adsorption because it is easy to obtain in the form of thin films, is reasonably inert, and forms SAMs of good quality [7, 9]. Thiols can form strong thiolate-Au bonds during the SAMs' formation [8], and these SAMs can be easily prepared in the liquid phase by the immersion of a substrate into an ethanolic thiol solution [9]. The high affinity of thiols to Au enables the creation of well-defined organic substrates with useful chemical functionalities and properties which can be changed in advance based on the application [9].

Kato *et al.* [42] reported the modification of Au disks or Au thin films deposited on cleaved mica with Im-C_{11}-SH SAMs for the design of a new conceptual electronic device. In other work, mixed SAMs containing Im-C_{11}-SH deposited on Au electrodes were characterized for the future development of biosensors or biocatalytic devices [43, 44].

Relevant literature on the interaction between various metal ions and different terminal functional groups of SAMs is summarized in Table 1.

Table 1. Interaction between metal ions and functional terminal groups of SAMs.

Metal ion	Functional terminal group of SAMs	Reference
Zn(II), Co(II), Ni(II)	-$C_3H_3N_2$ (Im)	[44]
K(I), Na(I), Cu(II), Ca(II), Mn(II), Fe(II), Fe(III), Co(II), Ni(II), Zn(II),	-COOH	[21, 45-47]
Cu(II)	-NH_2,	[46]
	-OH	
Cu(II), Pd(II), Pt(II), Cr(VI)	-C_5H_4N (Py)	[21], [48, 49]
Cu(II), Ni(II), Ag(I), Co(II), Ga(III), In(III)	-$(C_5H_3N)_2CH_3$ (Bpy)	[50-52]
Li(I)	-$C_{16}H_9$ (Pyr)	[53]
Pb(II), Cu(II)	EDTA	[54]
Ni(II)	NTA	[55]

Magallanes *et al.* [46] characterized the interaction between Cu(II) ions and carboxylic acid- or alcohol-terminated thiolate SAMs on Au(111) for the future preparation of heavy metal ion sensors. Ivanova *et al.* [48] reported the electrochemical deposition of monatomic-high layers of Pd(II) and Pt(II) on 4-mercaptopyridine SAMs on Au(111) electrodes. A new capacitor sensor was developed for the Cr(VI) determination by Kochana *et al.* [49]; in their work, an Au(111) electrode was functionalized with S-{12-[1-(pyridin-4-ylmethyl)-1H-1,2,3-triazol-4-yl]dodecyl} ethanethiolate SAMs with the functionals groups exhibiting an affinity to Cr(VI) anions. In the work of Zaitouna and Lai [44], Au disk electrodes were modified with mixed SAMs containing Im-C_{11}-SH. They were used to coordinate divalent metals such as Zn(II), Co(II), and Ni(II)

through the surface-immobilized imidazole terminal groups for the subsequent reversible immobilization of histidine-tagged peptides [44].

In this work, an imidazole-terminated alkanethiol was chosen for several reasons. The goal was to generate an alkanethiolate SAMs-based substrate with predefined properties of binding Ir and Rh from HCl solutions. First of all, it is well-known that imidazolium-based ionic liquids have already been used for Ir(IV) extraction from HCl solutions with high distribution ratios of up to 71.4 [56]. An assumption was made that the imidazole-terminated alkanethiol would be effective in the binding of Ir(IV) as well. On the other hand, Rh(III) is extracted by imidazolium-based ionic liquids to a lesser degree; the extraction efficiencies were reported to be less than 10% [57]. Nevertheless, we proposed to compare the surface saturation of Im-C_{11}-SH SAMs with these two metals. Secondly, Im-C_{11}-SH is a commercially available compound that simplifies the procedure of SAMs preparation. Thirdly, the literature review showed that several successful attempts were already made to prepare Im-C_{11}-SH SAMs on Au surfaces [42-44, 58]. All the facts mentioned above explain the choice of the thiol described above.

A second thiol, mercaptododecanoic acid (MDDA) was chosen to compare the metal adsorption on SAMs with different functional groups. The literature review illustrated that MDDA was successfully used to modify Au substrates and study the interaction with K^+/Na^+ in order to modulate the performance of SAM-GaIn-based molecular devices [45]. Also, MDDA SAMs and their metal complexes on Au substrates have recently been used in the work that can potentially speed up the development of high-performance molecular diode devices [47].

However, there have been no previous reports of the application of the Au(111) surfaces functionalized with Im-C_{11}-SH or MDDA SAMs for the sorption of Ir and Rh from liquid or gas phases. Therefore, in this paper, we report the sorption of Ir(IV) and Rh(III) from HCl solutions

on Im-C_{11}-SH and MDDA SAMs deposited on Au(111)-coated silicon and glass chips for the first time. The results of this work were important for designing new thiolate-functionalized Au-coated Si detectors that we successfully used for studying the sorption of online-produced radionuclides [59, 60]. The results of the online cyclotron-based experiments will be published in a separate paper that is currently in the last stages of preparation [61]. In the future, the upgraded functionalized detectors can potentially be used during online cyclotron-based experiments aimed at the characterization of the chemical properties of Mt.

2. Experimental section

2.1. Materials and equipment

Silicon wafers of 10 mm square size and 525 μm thick were coated with a 100 nm Au(111) film that had been primed with Ti (5 nm) to promote adhesion between SiO_2 and Au. Glass chips of aluminosilicate 10 mm square in size and 700 μm thick were coated with a 50 nm Au(111) film that had been primed with Ti (2.5 nm). Both coatings were performed by Platypus Technologies (Madison, Wisconsin, USA) using the e-beam evaporation technique. 1-(11-Mercaptoundecyl)imidazole (Im-C_{11}-SH, $C_{14}H_{26}N_2S$, 96% purity, Sigma-Aldrich, Milwaukee, Wisconsin, USA) and 12-mercaptododecanoic acid (MDDA, $C_{12}H_{24}O_2S$, 96% purity, Sigma-Aldrich, Milwaukee, Wisconsin, USA) were used without further purification. Hydrogen peroxide 30% (w/w) solution was purchased from VWR BDH®, Rouses Point, New York, USA. Undenatured ethanol (≥99.5% v/v) USP, 200 Proof, was purchased from by VWR, Spectrum Chemicals and Laboratory Products, Inc., Gardena, California, USA. Iridium Pure Plus Standard (1 μg/mL in 2% HCl) and Rhodium Pure Plus Standard (1 μg/mL in 2% HCl) were acquired from PerkinElmer, Inc., Shelton, Connecticut, USA. Iridium (10 μg/mL in 30% HCl) and Rhodium (10

μg/mL in 30% HCl) Calibration Standard was purchased from Inorganic Ventures, Christiansburg, Virginia, and used to prepare calibrators during INAA.

Im-C_{11}-SH and MDDA were weighed using a Mettler Toledo NewClassic MF ML204/03 balance with a precision of 0.1 mg. A commercially available SkinAct UV-sterilizer with a timer and a bulb emitting UV-light at 254 nm was used during the liquid-based hydrogen peroxide-mediated UV-photooxidation treatment.

2.2. Substrate pre-treatment

The procedure of precleaning the surface of Au-coated samples, and their regeneration after SAMs deposition was designed based on a surface regeneration technique developed by Johnson and Mutharasan [62], specifically a liquid-based H_2O_2-mediated UV-photooxidation (liquid-UVPO) treatment. Such a technique replaces a more aggressive and destructive method of Im-C_{11}-SH SAMs removal, involving a "piranha" solution [43].

A sample was placed into a Petri dish, and 170 μL of a 30% H_2O_2 solution was added to cover the whole surface area of the chip. The Petri dish was placed into the UV sterilizer, and the UV light was turned on for 30 min. After 30 min, the drop of H_2O_2 was refreshed to provide a high concentration of hydroxyl radicals. The Petri dish was placed back into the UV-sterilizer for an additional 30 min. Afterward, the chip was washed with a copious amount of a deoxygenated ethanol solution using a glass Pasteur pipette (around 10 times). The same procedure was used to remove thiolate SAMs from the surface during all experiments. To prepare the deoxygenated ethanol solution, ethanol was briefly heated in a water bath of a rotary evaporator at 55 °C for 15 min. The optimal rotation speed was 250 rpm.

2.3. Im-C_{11}-SH and MDDA solution preparation

Im-C_{11}-SH and MDDA must be stored in a desiccator and refrigerated at 2-8 °C to prevent their decomposition because their melting points are 26-31 °C and 45-50 °C, respectively [63, 64]. Before weighing Im-C_{11}-SH, the chemical must be kept at ambient temperature until it turns from a white solid into a homogeneous viscous liquid. MDDA is a white powder and stays in solid form at ambient temperature. To prepare a 1.6 mM or a 5 mM thiol solution, an appropriate amount of Im-C_{11}-SH or MDDA was weighed into a 15 mL centrifuge tube. To dissolve the thiol, 15 mL or 5 mL of a deoxygenated ethanol solution was added depending on the Im-C_{11}-SH or MDDA volume needed for experiments. The components were thoroughly mixed manually until a homogeneous solution was formed. The preparation procedure was performed in a fume hood at ambient temperature. The structural formulas of Im-C_{11}-SH is shown in Fig. 1.

a)

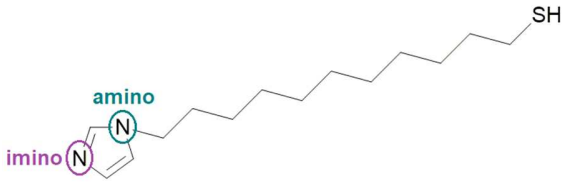

b)

Fig. 1 Structural formula of: (a) Im-C_{11}-SH (highlighted are amino and imino nitrogen sites of the imidazole ring); (b) MDDA used for the preparation of the thiol solutions.

2.4. Im-C_{11}-SH and MDDA SAMs formation

The procedure for SAMs deposition was designed based on the works of Yamamoto *et al.* [58], Kato *et al.* [42], and Wei *et al.* [43]. The precleaned chip was placed into the bottom of a 50 mL plastic tube using tweezers with plastic tips. To fully cover the chip, 3 mL of the prepared 1.6 mM or 5 mM ethanolic Im-C_{11}-SH solution was added. The plastic tube was wrapped with aluminum foil to avoid exposure to light. The cap of the tube was wrapped with Parafilm. The chip was submerged in the thiol solution for 21 h to ensure the formation of well-ordered, standing-up thiolate molecules in a closed-packed configuration with the highest coverage [7, 8]. The immersion procedure was performed in the fume hood at ambient temperature. The next day, the chip was taken out of the solution using the tweezers with plastic tips. It was washed with a copious amount of the deoxygenated ethanol solution using a glass Pasteur pipette (approximately 10 times). To dry the chip, a rubber bulb with a plastic tip was used to blow the residual drops off the surface. Then, a stream of compressed Ar gas was used to completely dry the surface.

The schematic structures of Im-C_{11}-SH and MDDA SAMs deposited on Au-coated Si and glass chips are represented in Fig. 2.

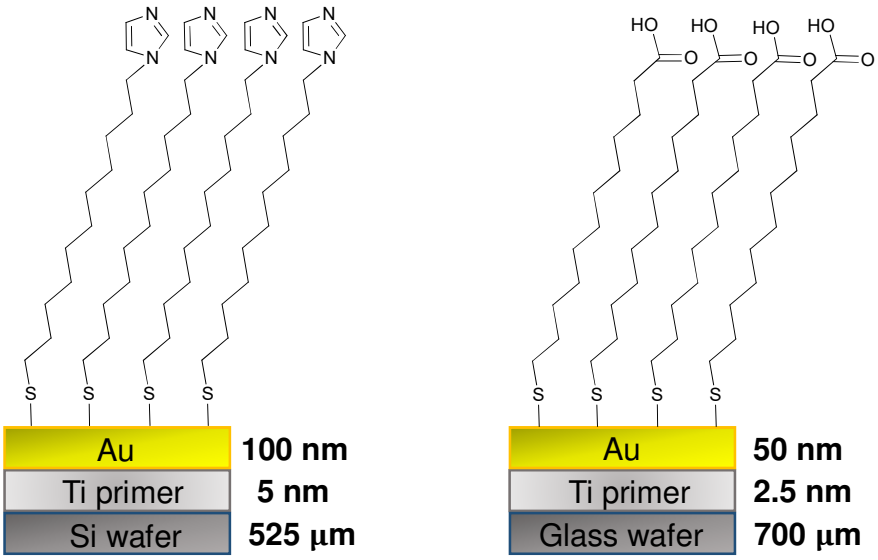

Fig. 2 Schematic diagram of the substrates investigated in this study. All chips were 10×10 mm^2.

The substrates were functionalized with Im-C_{11}-SH SAMs deposited from ethanolic thiol solutions with different concentrations. Experimental parameters such as usage of the liquid-UVPO treatment and a number of performed depositions were varied as well. Therefore, in this paper, Sample 1 refers to a 1.6 mM ethanolic Im-C_{11}-SH solution. The SAMs deposition from this solution was performed once. The chip was not precleaned with the liquid-UVPO treatment before the SAMs deposition.

Sample 2 refers to a 5 mM ethanolic Im-C_{11}-SH solution. The SAMs deposition from this solution was done for the second time. This means the Au surface was regenerated before the second deposition by removing the SAMs obtained during the first deposition from Sample 1. The liquid-UVPO treatment was used to remove the SAMs.

Sample 3 refers to a 5 mM ethanolic Im-C_{11}-SH thiol solution. The SAMs deposition from this solution was performed once. The chip was precleaned with the liquid-UVPO treatment before the SAMs deposition.

Sample 4 refers to a 5 mM ethanolic MDDA thiol solution. The SAMs deposition from this solution was performed once. The chip was precleaned with the liquid-UVPO treatment before the SAMs deposition.

Chips with freshly prepared SAMs were analyzed on the same day. To study the kinetics of the SAMs degradation via the XPS analysis, chips were stored in wafer carrier trays wrapped with aluminum foil to avoid exposure to light. The wafer carrier trays were placed in a box stored in a closed cabinet.

2.5. Ir(IV) and Rh(III) sorption on Au-coated substrates

Bare Au-coated chips, as well as Au-coated chips functionalized with Im-C_{11}-SH or MDDA SAMs, that were deposited from Sample 3 or Sample 4, respectively, were placed into 5 mL plastic tubes. Then, 2 or 3 mL of Ir(IV) and Rh(III) solutions of the target concentration in 0.55 M HCl were added separately into the 5 mL plastic tubes containing the chips. During the INAA analysis used to study the surface saturation of non-functionalized and Im-C_{11}-SH-functionalized chips, 2 mL of 5.2 μM Ir(IV) solution was added. Subsequently, for 0.5 μM, 1.0 μM Ir(IV) or 1.0 μM, 1.9 μM Rh(III) concentrations, 3 mL of the corresponding solution was added to simplify taking an aliquot needed for the INAA measurements. For the metal sorption from 0.5 μM, 5.2 μM Ir(IV) or 1.0 μM Rh(III) solutions, the non-functionalized and

Im-C_{11}-SH-functionalized silicon chips coated with 100 nm of Au were employed. For the metal sorption from 1.0 μM Ir(IV) or 1.9 μM Rh(III) solutions, the non-functionalized and Im-C_{11}-SH-functionalized glass chips coated with 50 nm of Au were used.

During the INAA analysis used to study the surface saturation of non-functionalized and MDDA-functionalized glass chips coated with 50 nm of Au, 3 mL of 0.5 μM or 5.2 μM Ir(IV) solutions was added.

During the NP-SIMS analysis, the metal sorption from 3 mL of 5.2 μM Ir(IV) or 9.7 μM Rh(III) solutions in 0.55 M HCl was performed on the non-functionalized and Im-C_{11}-SH-functionalized glass chips coated with 50 nm of Au. During both analyses, the non-functionalized and functionalized chips were left in contact with the metal solutions for approximately 21 h. The plastic tubes were wrapped with aluminum foil to avoid exposure to light. The cap of the tube was wrapped with Parafilm. The next day, the chips were taken out of the solutions using the tweezers with plastic tips. The solutions that were in contact with the functionalized chips overnight, as well as the solutions with the initial metal concentration were analyzed with INAA. Prior to the NP-SIMS analysis, the chips were washed with a copious amount of 0.55 M HCl solution using a glass Pasteur pipette (approximately 10 times). To dry the chips, a stream of compressed Ar gas was used.

2.6. Measurement techniques

Surface characterization techniques used for the measurement of the roughness, the surface coverage, the chemical state of the SAMs, the kinetics of the SAMs' degradation, the thickness of the SAMs, and the surface saturation with Ir(IV) are described below. Technical details of the employed techniques are provided in the Supplementary Material.

3. Results and discussion

3.1. Characterization of Im-C_{11}-SH and MDDA SAMs

3.1.1. Measurement of the coverage of Au-coated silicon chips with Im-C_{11}-SH SAMs

NP-SIMS was used to identify the presence of Im-C_{11}-SH SAMs on Au and measure the surface coverage with the organic molecules. The total mass spectra in Fig. 3a, and Figs. S1a-S3a in the Supplementary Material were acquired for the substrate which was submerged into Sample 1. The total mass spectra in Fig. 3b, and Figs. S1b-S3b in the Supplementary Material were acquired for the substrate which was submerged into Sample 2.

As mentioned in the Experimental Section in the Supplementary Material, the method of event-by-event bombardment-detection allows the selection of specific impacts, in the present case those involving SAM-related molecular fragments. In Fig. S1 in the Supplementary Material, the mass spectra contain characteristic peaks of the following Im-C_{11}-SH SAMs-Au fragments: hydrocarbon peaks $C_xH_y^-$, CN^-, S^-, SH^-, S_2^-, and $C_3N_2H_3CH^-$. The latter one is a product of the imidazole ring fragmentation. In Fig. 3, and Figs. S2-S3 in the Supplementary Material, the mass spectra contain characteristic peaks of the following Im-C_{11}-SH SAM-Au fragments: Au-S clusters Au_nS^- (229, 426, 623, 820, 1017 amu), $AuSC_xH_y^-$ (253, 255 amu), a deprotonated monomer (Im-C_{11}-S^-) (253.2 amu), and an Au-molecular cluster ion Au(Im-C_{11}-S^-)$_2$ (703 amu). Their observation verifies that Im-C_{11}-SH molecules are self-assembled on the surface of Au, forming the strong Au-S bond at the metal–thiol interface [65]. In Fig. 3b, their peak intensities are negligible compared to those in Fig. 3a.

Examining the zoomed-in region of 252.5-255.5 amu in Fig. 3a and Fig. 3b, the important characteristic peak of an (Im-C_{11}-S^-) fragment at 253.2 amu corresponds to the deprotonated molecule of Im-C_{11}-SH. The adsorption of thiols on the Au surface occurs in two steps, beginning with physisorption followed by chemisorption [8]. During the latter one, the thiol molecule becomes deprotonated, converting into the thiolate (Im-C_{11}-S−Au). The adsorption process can be described as follows:

$$\text{Im-}C_{11}\text{-SH} + \text{Au} \rightarrow (\text{Im-}C_{11}\text{-SH})_{phys}\text{Au} \quad (1)$$

$$(\text{Im-}C_{11}\text{-SH})_{phys}\text{Au} \rightarrow \text{Im-}C_{11}\text{-S}-\text{Au} + \tfrac{1}{2}H_2 \quad (2)$$

It must be noted that for the substrate shown in Fig. 3a, the concentration of an Im-C_{11}-SH solution was 1.6 mM, whereas, in Fig. 4b, it was increased to 5 mM. As a result, the intensity of the (Im-C_{11}-S^-) peak increased with an increase in the thiol concentration. This is one of the pieces of evidence that the coverage increased.

Also, in Fig. 3a the surface of Au was not precleaned using the liquid-UVPO treatment before the SAMs deposition unlike the substrate shown in Fig. 3b. The positive impact of this treatment can be observed by comparing spectra in Fig. 3a and Fig. 3b in the mass ranges 121-183 amu and above 255.2 amu. All peaks in these regions correspond to contaminants in the form of adventitious organic compounds adsorbed on the surface of Au either during the manufacturing of the Au-coated Si chips or during their handling under ambient laboratory conditions. Such compounds are composed of polymeric hydrocarbon species, $(C_xH_y)_n$, or oxidized carbon species, C_mO_p, containing C–O–C, O=C–O, O=C=O, and C–OH groups [66, 67].

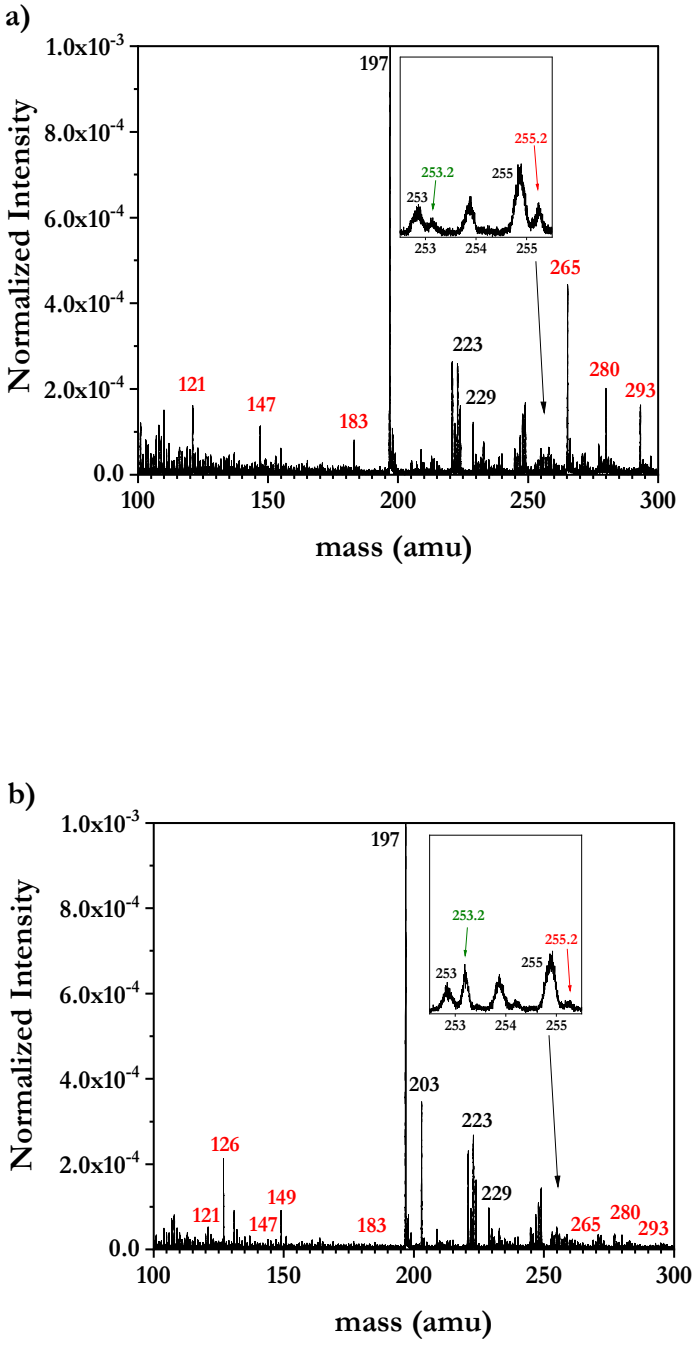

Mass (amu)	Fragment
121-183	contaminants
197	Au^-
203	contaminants
223	$AuC_2H_2^-$
229	AuS^-
253	$AuSC_2^-$
253.2	Im-C_{11}-S^-
255	$AuSC_2H_2^-$
255.2	contaminants
265	
280	
293	

Fig. 3 (a) Mass spectrum of non-precleaned Au functionalized with Im-C_{11}-SH SAMs deposited from Sample 1. (b) Mass spectrum of precleaned Au functionalized with Im-C_{11}-SH SAMs deposited from Sample 2.

The same trend can be observed in the spectra of higher mass regions in Fig. S2a and Fig. S2b in the Supplementary Material. The intensities of the peaks at 311.2-365.2 amu and 485.2 amu decrease significantly after the liquid-UVPO treatment was used. This technique was selected for all further experiments due to its efficacy, and its promising preservation of surface morphology as well as crystallinity of Au [62].

To measure the coverage (*K*) of Au-coated Si chips with Im-C_{11}-SH SAMs, the Surface Analysis and Mapping of Projectile Impacts (SAMPI©) software (version 5.0.5) was employed [68, 69]. A characteristic pair of Au-S cluster ions, namely Au_2S^- (426 amu) and Au_3S^- (623 amu), was selected to perform calculations. The SAMPI© software enables the extraction of the total number of detected ions per impact ($Y_{tot,}$ the total yield) from a total spectrum, and the number of detected ions per impact when detecting a specific ion ($Y_{coinc,}$ the coincidence yield) from a coincidence spectrum. In general, a coincidence spectrum is composed of events containing a selected ion of interest. It shows all ions co-emitted with the selected ion from the same desorption volume [69-73]. In the present case, impacts of the detected Au_3S^- ions were selected to obtain a coincidence spectrum, after which the total yield of the co-emitted Au_2S^- ion, $Y_{tot}\ (Au_2S^-)$, was divided by the coincidence yield of Au_2S^- ion, $Y_{coinc}\ (Au_2S^-)$:

$$K = \frac{Y_{tot}\ (Au_2S^-)}{Y_{coinc}\ (Au_2S^-)} \cdot 100\% \qquad (3)$$

The corresponding peaks are shown in Fig. S2a and Fig. S3a in the Supplementary Material. *K* was measured to be (78 ± 7)% when the SAMs deposition was performed from Sample 1.

The *K* value increased when the SAMs deposition was performed from Sample 2 which had a higher thiol concentration. Impacts of the detected Au_3S^- (623 amu), $Au(Im\text{-}C_{11}\text{-}S^-)_2$ (703 amu, and 704 amu due to the presence of ^{13}C), Au_4S^- (820 amu), Au_5S^- (1017 amu) ions were selected to obtain a sum coincidence spectrum. The corresponding peaks are depicted in

Fig.S3b in the Supplementary Material. In general, a sum coincidence spectrum is composed of events containing either of the selected ions of interest. Such selection enhances the accuracy of co-localized species identification on complex surfaces [69]. To measure *K*, the total yield of Au_2S^- ion was divided by the coincidence yield of Au_2S^- ion utilizing Eqn. (3). The corresponding peak is shown in Fig. S2b in the Supplementary Material. The *K* value was increased to (99 ± 6)%. The reported errors are statistical errors of NP-SIMS measurements.

Moreover, the appearance of another characteristic peak of a dimer $Au(Im\text{-}C_{11}\text{-}S^-)_2$ at 703 amu in Fig. S3b in the Supplementary Material confirms that the coverage increased when a more concentrated thiol solution was used. The reason is that this peak corresponds to the fragment where two deprotonated molecules of $Im\text{-}C_{11}$-SH are attached to the same Au center.

Additionally, one more confirmation that the coverage increased is we observed a decrease in the peak intensities corresponding to the substrate signal Au^-, and Au cluster ions Au_x^- shown in Fig. 3b, and Figs. S2b-S3b in the Supplementary Material. If there is a monolayer of thiol molecules present on the Au surface, it is harder for projectiles to bombard the Au surface deeply. Consequently, part of the projectiles' energy is lost for the SAMs fragmentation. This results in decreasing the peak intensities of Au^- (197 amu), Au_2^- (394 amu), Au_3^- (591 amu), Au_4^- (788 amu), Au_5^- (985 amu) ions.

The main conclusions of NP-SIMS are: 1) a chip needs to be precleaned using the liquid-UVPO treatment before the SAMs deposition from a 5 mM ethanolic thiol solution; 2) The highest value of the coverage was obtained in the order of (99 ± 6)% after the second SAMs deposition which indicates that surface is covered with $Im\text{-}C_{11}$-SH SAMs quantitatively. To sum up, to obtain the highest coverage, one cycle of SAMs deposition-regeneration is recommended before the final second deposition.

3.1.2. Evaluation of the roughness of non-functionalized and functionalized Au-coated silicon chips

AFM was employed to evaluate the roughness of the bare Au surface (*i.e.*, after precleaning using the liquid-UVPO treatment), and Au substrates functionalized with Im-C_{11}-SH SAMs deposited from Sample 3. The AFM images (10 × 10 μm^2) are shown in Fig. 4, and Fig. S4a in the Supplementary Material, respectively.

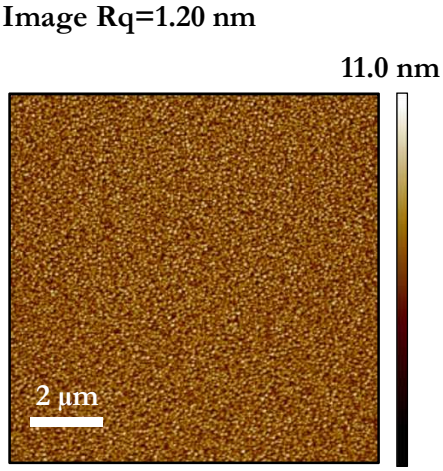

Fig. 4 AFM image (10 × 10 μm^2) of pure precleaned Au.

Image Rq is the root mean square average of the profile heights over the evaluation length, which gives information about the surface roughness. For each sample, three different areas were scanned, and the surface roughness value was averaged. The Image Rq value for the bare Au surface is 1.20 nm as shown in Fig. 4. The AFM studies performed by Weiss *et al.* [74, 75] showed that the lowest surface roughness results in the formation of well-ordered SAMs with a high degree of coverage due to a minimal degree of structural defects. Thus, the surface roughness of the Au substrates used in this study is sufficient to obtain well-ordered, densely packed SAMs. The surface roughness of Au subsequently functionalized with Im-C_{11}-SH SAMs is 1.20 nm as illustrated in Fig. S4a in the Supplementary Material. As will be discussed later,

the chips were tested for whether they can be reused by using the liquid-UVPO treatment [62] to remove SAMs, and depositing SAMs for a second time. The roughness was also evaluated for the substrate functionalized with Im-C_{11}-SH SAMs deposited from Sample 2. The Image Rq value of this substrate is 1.25 nm as depicted in Fig. S4b in the Supplementary Material. The comparison of the similar AFM images and the Image Rq values, which remain in the same range, suggests that the first and the second SAMs depositions, as well as the liquid-UVPO treatment, do not produce a macroscopic change to the surface morphology and topography, and as a result, the substrates can be reused without noticeable surface damage.

In the corresponding 2 × 2 μm^2 AFM images provided in Figs. S5a-c in the Supplementary Material, the grains of Au can be observed.

3.1.3. The study of the Im-C_{11}-SH and MDDA SAMs' chemical state and the kinetics of their degradation

The chemical state of Im-C_{11}-SH SAMs deposited from Sample 3 was characterized by XPS. Fig. 5 and 6 show the XPS spectra of the S 2p and N 1s regions of the SAMs. Table 2 summarizes peak areas as well as the elemental composition of SAMs. Sulfur XPS spectra shown in Fig. 5, and Fig.S7 in the Supplementary Material contain spin-orbit splitting components with S $2p_{3/2}$ at approximately 162.5 eV which corresponds to a thiolate bound to the Au surface, while S $2p_{1/2}$ at 163.0-164.0 eV indicates some unbound sulfur species produced due to damage to the SAMs caused by the ionizing radiation (X-rays during XPS measurements, or UV-light during the liquid-UVPO treatment) [42, 76-78].

Nitrogen XPS spectra are presented in Fig. 6, and Fig. S7 in the Supplementary Material for the same series of samples. They contain two components with N 1s peaks at 399.42 and

401.19 eV, which are assigned to imino and amino N of the imidazole ring in the Im-C_{11}-SH molecule depicted in Fig. 1. [15, 42, 79].

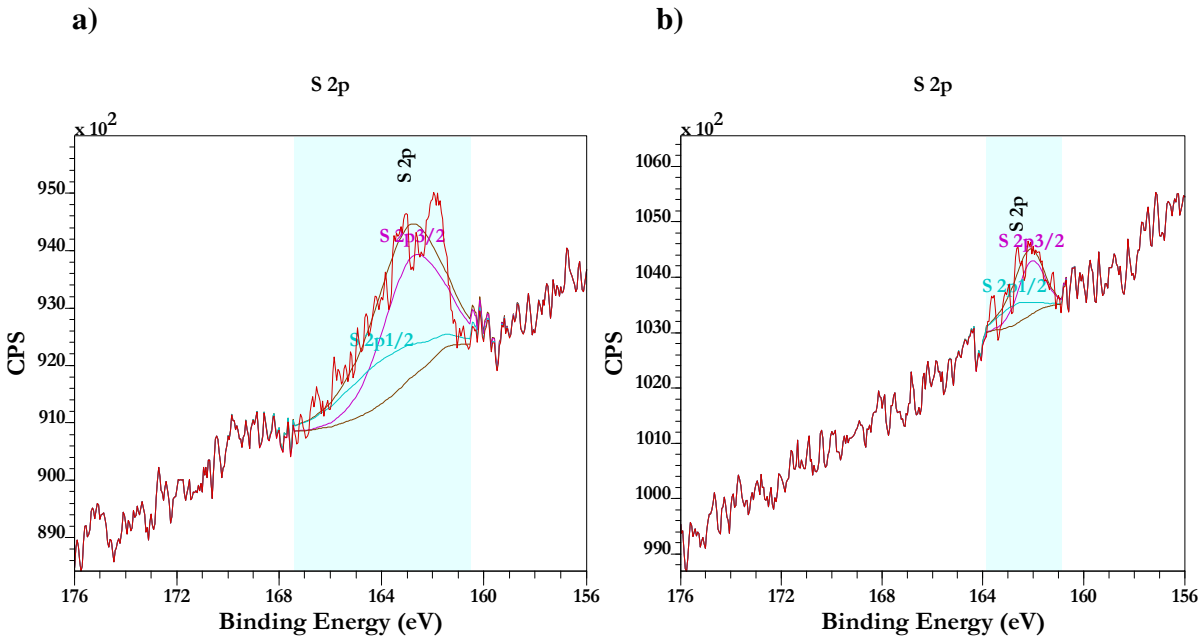

Fig. 5 Sulfur 2p XPS for Im-C_{11}-SH SAMs on precleaned Au: (a) the fresh SAMs deposited from Sample 3; (b) SAMs removed using the liquid-UVPO treatment.

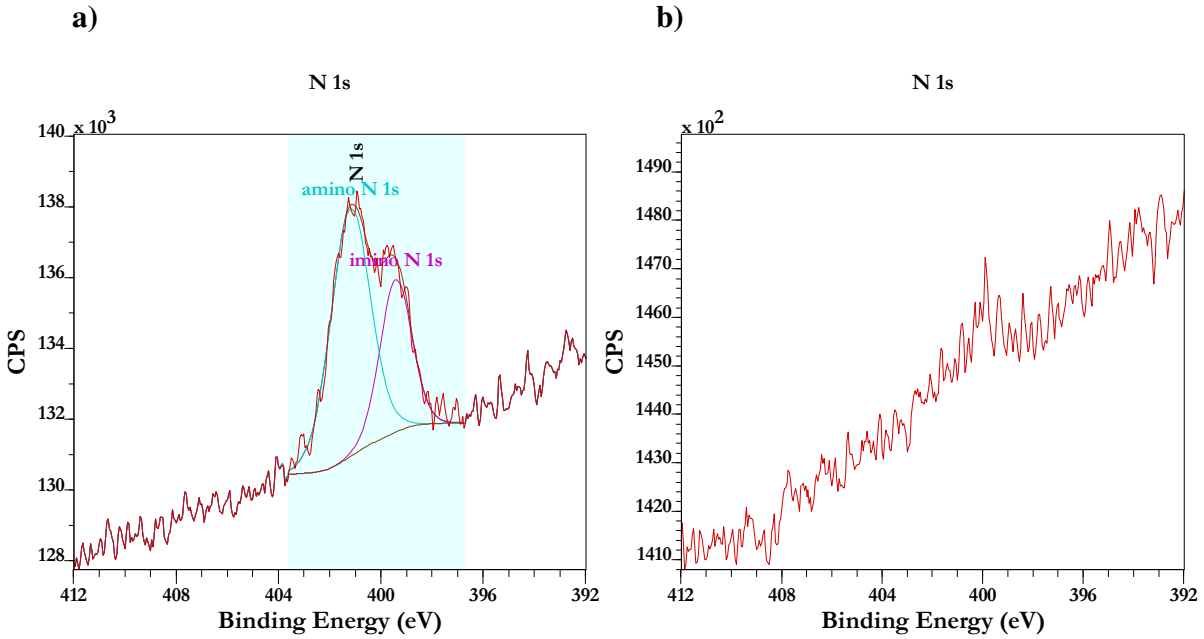

Fig. 6 Nitrogen 1s XPS for Im-C_{11}-SH SAMs on precleaned Au: (a) the fresh SAMs deposited from Sample 3; (b) SAMs removed using the liquid-UVPO treatment.

Table 2. Peak areas in the XPS spectra, and elemental composition of Im-C_{11}-SH SAMs.

Sample	Au 4f, CPS eV	C 1s, CPS eV	N 1s, CPS eV	O 1s, CPS eV	S 2p, CPS eV	Au 4f, %	C 1s, %	N 1s, %	O 1s, %	S 2p, %	Desorbed SAMs, %
Freshly deposited	1621.82	2474.20	295.92	334.40	131.24	33.39	50.93	6.09	6.88	2.70	0
2 weeks of storage	1802.662	2772.53	333.30	378.65	127.14	33.29	51.21	6.16	6.99	2.35	3
1 month storage	1854.864	2794.45	263.08	411.92	119.05	34.08	51.34	4.83	7.57	2.19	9
After SAMs removal	2979.337	1312.58	-	268.91	26.76	64.94	28.61	-	5.86	0.58	80

As can be seen in Fig. 5b, Fig. 6b, and Table 2, the peaks of S 2p and N 1s vanished after the H_2O_2-mediated liquid UV-light photooxidation treatment that was employed to remove thiolate SAMs. Additionally, increases in the Au 4f peak intensity shown in Fig. S6b in the Supplementary Material, and the Au 4f peak area shown in Table 2 further support this idea. So, when SAMs are removed, the Au photoelectrons are no longer attenuated which raises the intensity of the Au 4f peaks [76]. The atomic fractions of S, C, and N decrease drastically after the Im-C_{11}-SH SAMs are removed. The intensities and the peak areas of S 2p, C 1s, and N 1s peaks are related to the amount of Im-C_{11}-SH SAMs present on the Au surface. Decreases in the intensities, the peak areas, and the atomic fractions explain Im-C_{11}-SH SAMs desorption [76]. Carbon XPS spectra are illustrated in Figs. S6-S7 in the Supplementary Material. The peak area of the S 2p peak of the freshly prepared Im-C_{11}-SH SAMs was assumed to be 100%. After the

SAMs' removal, the peak area of the S 2p peak was 20% of the original 100%. This suggests that 80% of the SAMs were desorbed from the Au surface after using the H_2O_2-mediated liquid UV-light photooxidation treatment. All of this suggests that the Au-coated Si chips can be reused.

The process that stands behind the removal of SAMs from the Au surface is the following. After the UV light interacts with H_2O_2, hydroxyl radicals ($HO^{\bullet}$) are formed. Then, thiolate species are oxidized to sulfonates that loosely bind to metal surfaces and can be easily washed away with ethanol [62]:

$$\tfrac{1}{2}\, H_2O_2 + h\nu \rightarrow HO^{\bullet} \qquad (4)$$

$$RS{-}Au + O_2 + HO^{\bullet} \rightarrow RSO_3H + Au \qquad (5),$$

where R is the organic radical.

Furthermore, the effect of sample aging was studied. The XPS results indicate that prepared SAMs do not degrade significantly when stored under ambient conditions, except that samples were stored in wafer carrier trays and wrapped with aluminum foil to avoid exposure to air and light. These are known to be the main factors in causing SAMs' degradation [76]. The decrease in the peak areas of the S 2p peaks allows us to evaluate the kinetics of the Im-C_{11}-SH SAMs degradation, and 3% and 9% of SAMs were lost after two weeks and one month of storage, respectively. Additionally, a shoulder that corresponds to the imino N component becomes less pronounced after sample storage as shown in Figs. S7a,b in the Supplementary Material. This can be attributed to the transformations inside the imidazole ring due to the atmospheric oxidation which was previously reported by Safaei *et al.* [80]. On the other hand, the intensities the Au 4f peaks illustrated in Figs. S7a,b in the Supplementary Material and the Au 4f peak areas listed in Table 2 increase during sample storage which also means that a lower amount of the thiolate molecules is present on the Au surface. Table 2 also reveals the same

trend for the elemental composition of SAMs. Degradation of thiolate SAMs under ambient conditions leads to the formation of either disulfides (Eqn. 6) or sulfonates (Eqn. 7) which can be easily washed away from the Au surface with ethanol [8, 81, 82]:

$$2\ RS{-}Au \rightarrow RSSR + 2\ Au \qquad (6)$$

$$RS{-}Au + H_2O + O_3 \rightarrow RSO_3H + HO{-}Au \qquad (7)$$

Similarly, the chemical state of MDDA SAMs deposited from Sample 4 was characterized by XPS. The sulfur XPS spectra shown in Fig. 7 contain S $2p_{3/2}$ and S $2p_{1/2}$ spin-orbit splitting components.

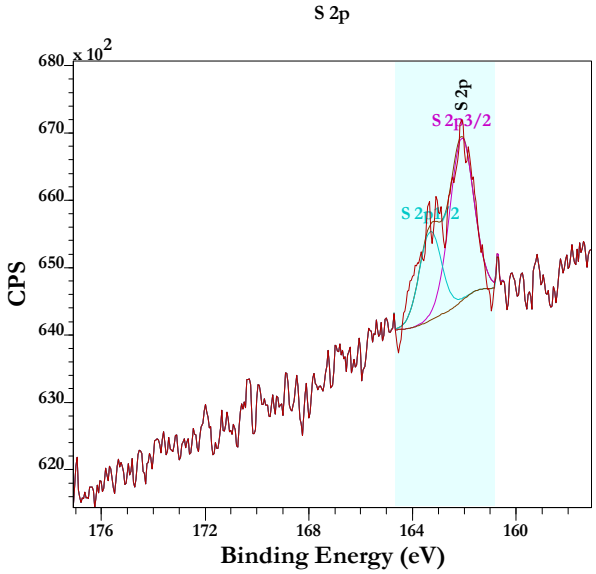

Fig. 7. Sulfur 2p XPS for the fresh MDDA SAMs deposited from Sample 4 on precleaned Au.

Carbon XPS spectra contain the C-C, C-H component at 284.8 eV due to the presence of a hydrocarbon chain, the C-O-C component at 286 eV, and the O-C=O component at 288.5 eV as depicted in Figure S9 in the Supplementary Material [78], [83]. The last two components are attributed to the presence of the carboxyl functional group in the MDDA structure shown in Figure 1b. Table S2 summarizes the Au 4f, C 1s, O 1s, S 2p peak areas as well as the elemental

composition of SAMs. Gold and oxygen XPS spectra are illustrated in Figure S10 in the Supplementary Material.

The effect of sample aging was studied under the same storage conditions as for Im-C_{11}-SH SAMs. Minor changes in the shape of the S 2p doublet peak and the S 2p peak area shown in Figure S8 and Table S2 in the Supplementary Material indicate the non-significant degradation of MDDA SAMs during sample storage. The Au 4f peak area also remained approximately unchanged after one week of the sample storage as shown in Table S2 in the Supplementary Material. Slight increases in the Au 4f peak area and the Au 4f peak intensity as seen in Table S2 and Figure S10 in the Supplementary Material after one month of sample storage mean that some MDDA SAMs were desorbed from the surface of Au, making the Au photoelectrons no longer attenuated [76]. The C 1s peak intensity and the C 1s peak area presented in Figure S9 and Table S2 in the Supplementary Material decrease slightly after one month of the sample storage, also supporting the idea of the insignificant MDDA SAMs' degradation.

3.1.4. Measurement of the thickness of Im-C_{11}-SH SAMs

Ellipsometry is an optical spectroscopy technique that was used to determine the thickness of the Im-C_{11}-SH SAMs deposited from Sample 3. Ellipsometry is sensitive to the presence of thin SAMs on the surface of Au due to the change in the measured delta (Δ) parameter, which contains information about the phase difference between p- and s-polarized light [84]. The measured (square, triangle, and circle symbols) and modeled (dash dot, dot, and dash curves) Δ values versus the wavelength (λ) are shown in Fig. S11 in the Supplementary Material. During ellipsometry measurements, it is important to measure a bare Au surface to determine optical constants at first. The obtained data are shown as green square symbols in Fig.

8 and were fitted using the B-Spline layer. As a result, the modeled green dash dot curve in Fig. 8 represents the bare precleaned Au surface. The blue triangle symbols in Fig. 8 represent Im-C_{11}-SH SAMs on the precleaned Au surface. These data were used to determine the thickness of the Im-C_{11}-SH SAMs. Fig. 8 shows a detail of the low-Δ values where the change between the bare precleaned Au surface and the functionalized surface is observed. One can notice a vertical shift in Δ toward lower values which is attributed to the presence of a thin film on top of Au [84]. In the case of thicker films on the Au surface, a larger shift is observed [84].

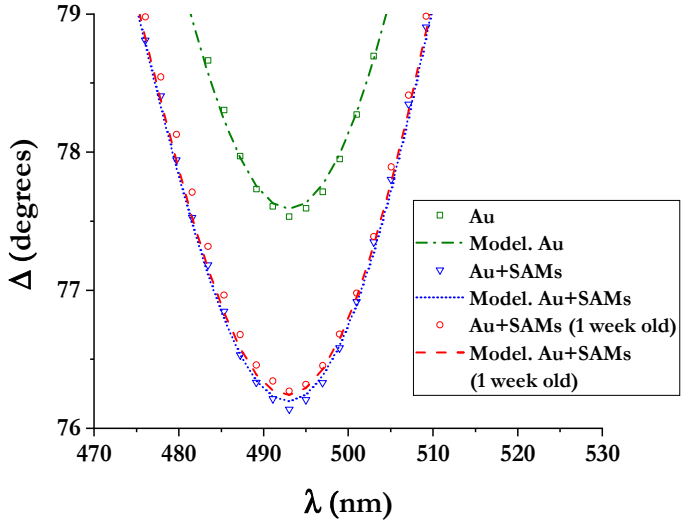

Fig. 8 Detail of low-delta values as a function of wavelength from ellipsometry: measured (square, triangle, and circle symbols) and modeled (dash dot, dot, and dash curves) data for bare precleaned Au (green), fresh Im-C_{11}-SH SAMs deposited from Sample 3 on precleaned Au (blue), and Im-C_{11}-SH SAMs on precleaned Au after one week of storage (red). The B-spline layer was used to fit the bare precleaned Au data with n=1.50. The Cauchy layer was used to fit the Im-C_{11}-SH SAMs data with n=1.450.

By fitting the data using the Cauchy layer, the blue dot curve was obtained, and the thickness of 1.690 ± 0.014 nm was determined for the freshly deposited Im-C_{11}-SH SAMs. The measured thickness value indicates the presence of a single monolayer on the surface of Au and is in good agreement with the literature results obtained for similar films [14-16].

The thickness of Im-C_{11}-SH SAMs on the precleaned Au surface was also measured after one week of sample storage using the data represented by the red circle symbols in Fig. 8. The red dash curve was obtained after fitting the data, and a thickness of 1.640 ± 0.011 nm was determined. The thickness is slightly lower than that for the freshly deposited SAMs, but the difference in values is practically insignificant. Fig. 8 also demonstrates the proximity of the fits for the freshly deposited and one-week-old SAMs. As a result, ellipsometry showed that storing Im-C_{11}-SH SAMs for one week did not initiate degradation processes which would lead to a decrease in the SAMs thickness. The uncertainties are reported at the 90% confidence level calculated by the fit algorithm [13].

3.2. Ir(IV) and Rh(III) sorption on Au-coated substrates

3.2.1. Measurement of the coverage of non-functionalized and functionalized Au-coated chips with Ir(IV) and Rh(III)

In the following section, the results of the NP-SIMS and the INAA analyses utilized to study the sorption of Ir(IV) and Rh(III) from 0.55 M HCl solutions on non-functionalized and functionalized Au-coated chips are discussed.

During the NP-SIMS analysis, metal sorption from 5.2 μM Ir(IV) and 9.7 μM Rh(III) solutions in 0.55 M HCl was performed on non-functionalized Au-coated glass chips and Au-coated glass chips functionalized with Im-C_{11}-SH SAMs deposited from Sample 3. The substrates were submerged in Ir(IV) and Rh(III) solutions for approximately 21 h.

In the NP-SIMS analysis, a primary beam of 520 keV Au_{400}^{4+} clusters bombards the surface of the functionalized chips, and the energy transfer from the beam to the surface causes the emission of negatively charged cluster ions [69, 85]. Fig. 9, and Figs. S12a-c in the Supplementary Material display characteristic peaks of $RhCl_3^-$ (208-214 amu), $RhCl_4^-$ (243-251

amu), $RhCl_5^-$ (278-284 amu), $Rh_2Cl_7^-$ (451-459 amu), $Rh_3Cl_4H^-$ (450-458 amu) clusters which indicate the sorption of Rh(III) on functionalized Au-coated glass chips. $Rh_xCl_y^-$ introduce groups of peaks in the mass spectra due to the isotopes of Cl.

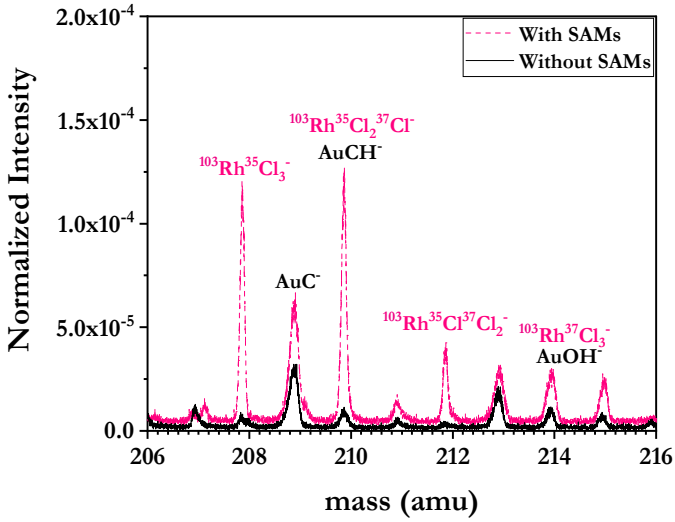

Fig. 9 Mass spectra of precleaned Au functionalized with Im-C_{11}-SH SAMs from Sample 3 and sorbed Rh(III) (pink line), and precleaned non-functionalized Au with sorbed Rh(III) (black line). $[Rh]_{init}$ = 9.7 μM , [HCl] = 0.55 M. Mass range of 206 – 216 amu showing ions of $RhCl_3^-$ clusters and their interference with other ions.

In Fig. 9 and Figs. S12a-c in the Supplementary Material, the intensities of these clusters are much higher for samples where the Rh(III) sorption occurred on Au-coated glass chips functionalized with Im-C_{11}-SH SAMs compared to non-functionalized ones. For instance, the sum net yield for the peaks corresponding to $RhCl_3^-$ clusters (208-214 amu) observed on precleaned Au functionalized with Im-C_{11}-SH SAMs, and precleaned Au without Im-C_{11}-SH SAMs is 1.73×10^{-2}, and 1.85×10^{-3}, respectively. The net yield is the total yield with the background subtracted. The difference of one order of magnitude indicates more quantitative Rh(III) sorption on functionalized Au-coated glass chips rather than on non-functionalized ones.

$RhCl_3^-$ was chosen as a primary cluster to measure *K* of Im-C_{11}-SH SAMs with Rh(III). This cluster gives a more accurate result since its peaks are more narrow and have no significant

interference compared to the $RhCl_4^-$ group of peaks, which have more interference with other ions, such as $AuCNC_2^-$ (247 amu) and $AuCNC_2H^-$ (248 amu) shown in Fig. S12b. $RhCl_5^-$ and $Rh_2Cl_7^-$ clusters were not taken into consideration for the coverage calculation due to low statistics.

To measure *K* of Im-C_{11}-SH SAMs with Rh(III), a similar approach described above to measure *K* of Au-coated Si chips with Im-C_{11}-SH SAMs was used [69-73]. At first, impacts of the detected $^{103}Rh^{35}Cl_2{}^{37}Cl^-$ ions (210 amu) were selected to obtain a coincidence spectrum. After this, the total yield of $^{103}Rh^{35}Cl_3^-$ ion (208 amu), Y_{tot} ($^{103}Rh^{35}Cl_3^-$), was divided by the coincidence yield of $^{103}Rh^{35}Cl_3$ ion (208 amu), Y_{coinc} ($^{103}Rh^{35}Cl_3^-$):

$$K = \frac{Y_{tot}\,(^{103}Rh^{35}Cl_3^-)}{Y_{coinc}\,(^{103}Rh^{35}Cl_3^-)} \cdot 100\% = \frac{0.008055}{0.009912} \cdot 100\% = 81.3\% \quad (8)$$

K was measured to be (81.3 ± 3.8)%. There were not enough statistics to measure the coverage of non-functionalized Au with $RhCl_3^-$ clusters. The reported error is a statistical error of NP-SIMS measurements.

In the Rh(III) sorption experiments, the coverage of Au with Im-C_{11}-SH SAMs was measured according to Eqn. (3) and gave a result of (80 ± 5)%. This coverage was measured after the sample had been in contact with Rh(III) solution in 0.55 M HCl. This means that there is no Im-C_{11}-SH SAMs degradation upon contact with dilute acids.

The discussion of Ir(IV) sorption results is presented in the Supplementary Material and shown in Fig. S13 and Table S3. A triply charged complex $[RhCl_6]^{3-}$ and a doubly charged complex $[IrCl_6]^{2-}$ are predominant species in given solutions [86, 87]. The fact that we observe $Rh_xCl_y^-$ and $Ir_xCl_y^-$ clusters in the NP-SIMS spectra of the functionalized Au after the contact with Rh(III) and Ir(IV) solutions indicates that chlorocomplexes of the named metals are sorbed

on the Im-C_{11}-SH SAMs on Au. The in-depth analysis of the binding affinity of the metal chlorocomplexes and the kinetics of complex formation was outside of the scope of this paper.

3.2.2. Measurement of the surface saturation of non-functionalized and functionalized Au-coated chips with Ir(IV)

During the INAA analysis, the initial Ir(IV) concentration was varied in the range of 0.5 – 5.2 μM in 0.55 M HCl to study the surface saturation of Au-coated silicon or glass chips functionalized with Im-C_{11}-SH SAMs deposited from Sample 3, and non-functionalized Au-coated chips. The substrates were submerged in Ir(IV) solutions for approximately 21 h. The molar mass of Ir (192.217 g/mol) was used to measure the molar concentration of Ir(IV) in the aqueous phase.

The surface saturation (SS) of Im-C_{11}-SH SAMs with Ir(IV) was measured using the following equation:

$$SS = \frac{C_{\mathrm{Ir\,init}} - C_{\mathrm{Ir\,eq}}}{A \cdot N_{\mathrm{Im}-C_{11}-\mathrm{SH}}} \cdot 100\% = \frac{(C_{\mathrm{Ir\,init}} - C_{\mathrm{Ir\,eq}}) \cdot V_{\mathrm{Ir}} \cdot N_A}{A \cdot N_{\mathrm{Im}-C_{11}-\mathrm{SH}}} \cdot 100\% = \tag{9}$$

$$= \frac{N_{\mathrm{Ir\ init}} - N_{\mathrm{Ir\ eq}}}{A \cdot N_{\mathrm{Im}-C_{11}-\mathrm{SH}}} \cdot 100\% = \frac{\Delta N_{\mathrm{Ir}}}{A \cdot N_{\mathrm{Im}-C_{11}-\mathrm{SH}}} \cdot 100\%,$$

where $C_{\mathrm{Ir\,init}}$ is the measured concentration of Ir(IV) solutions in 0.55 M HCl before sorption, $C_{\mathrm{Ir\,eq}}$ is the measured concentration of Ir(IV) solutions in 0.55 M HCl after sorption, V_{Ir} is the the volume of Ir(IV) solutioßns that were in contact with the substrates, N_A is the Avogadro constant, $N_{\mathrm{Ir\ init}}$ is the initial number of Ir(IV) molecules in solution before sorption, $N_{\mathrm{Ir\ eq}}$ is the number of Ir(IV) molecules in solution after sorption, ΔN_{Ir} is the difference of the number of Ir(IV) molecules in solution before and after sorption, A is the area of a chip that is equal to 1 cm^2, $N_{\mathrm{Im}-C_{11}-\mathrm{SH}}$ which equals 4.5×10^{14} molecules/cm^2 is the typical surface density of molecules for alkanethiolate SAMs when the maximum coverage is obtained [9].

Fig. 10 illustrates that the surface saturation of Im-C_{11}-SH SAMs with Ir(IV) increases with an increase of the initial Ir(IV) concentration. A possible reason is that there is no driving force for the sorption to occur on the surface when the initial Ir(IV) concentration is too low. The higher initial Ir(IV) concentration results in Ir(IV) sorption on the substrate surface. The highest surface saturation of (77 ± 12)% was obtained with a 5.4 μM initial Ir(IV) concentration. The uncertainties, which are primarily determined by the counting precision, are reported at the 1σ (68% confidence level).

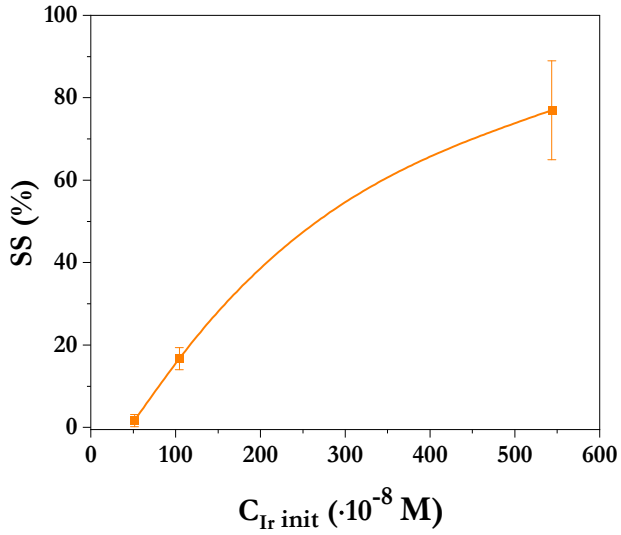

Fig. 10 The surface saturation (SS) of Im-C_{11}-SH SAMs with Ir(IV) as a function of the initial concentration of Ir(IV) solutions in 0.55 M HCl. The line is drawn to guide the eye. The uncertainties are at the 1σ (68% confidence level).

INAA results for functionalized and non-functionalized Au-coated chips are summarized in Table 4, and Table S4 in the Supplementary Material, respectively. Ir(IV) was barely adsorbed on precleaned Au-coated chips without SAMs, which can be seen in Table S4 in the Supplementary Material, and the highest surface saturation of <20% was observed with a 5.4 μM initial Ir(IV) concentration.

Table 4. The measured concentration of Ir(IV) solutions in 0.55 M HCl before and after sorption, and comparison of the surface saturation of Im-C_{11}-SH-functionalized Au-coated chips with Ir(IV). The uncertainties are at the 1σ (68% confidence level).

	Substrate		
	Im-C_{11}-SH SAMs on precleaned Au-coated chips		
$C_{\text{Ir init}}$ ($\cdot 10^{-8}$ M)	51.35 ± 0.26[a]	104.4 ± 0.5[b]	543.1 ± 3.2[a]
$C_{\text{Ir eq}}$ ($\cdot 10^{-8}$ M)	50.93 ± 0.26	100.2 ± 0.5	514.3 ± 3.1
V_{Ir} ($\cdot 10^{-3}$ L)	2	3	3
ΔN_{Ir} ($\cdot 10^{14}$ molecules)	0.08 ± 0.07	0.75 ± 0.12	3.5 ± 0.5
$N_{\text{Im-C}_{11}\text{-SH}}$ ($\cdot 10^{14}$ molecules/cm^2) [9]	4.5		
SS (%)	1.7 ± 1.5	16.7 ± 2.7	77 ± 12

a - Si chip coated with 100 nm of Au, b - glass chip coated with 50 nm of Au, other quantities are defined in the main text.

INAA was also performed to study the Rh sorption, but the uncertainties of the measurements were very high. The cross-sections of the ^{191}Ir(n,g)^{192}Ir and the ^{103}Rh(n,g)^{104m}Rh reactions performed during the INAA analysis are 954 ± 10 b and 145 ± 2 b, respectively [88]. The difference of approximately one order of magnitude can explain the lower production of ^{104m}Rh compared to ^{192}Ir as well as the lower number of counts in the ^{104m}Rh photopeak as shown in Fig. S14 in the Supplementary Material. Additionally, the gamma-ray branching ratio for ^{104m}Rh, which is 48% [89], is much lower than that for ^{192}Ir which is 83% [90]. All of the factors explain the increased uncertainties during Rh measurements.

Similarly, the surface saturation with Ir(IV) was studied on Au-coated glass chips functionalized with MDDA SAMs deposited from Sample 4, and non-functionalized ones. The substrates were submerged in Ir(IV) solutions with concentrations of 0.5 and 5.2 μM in 0.55 M HCl for approximately 21 h. The results are summarized in Table 5 and show that the highest surface saturation of (84 ± 16)% was measured with a 5.4 μM initial Ir(IV) concentration. The surface saturation increases with an increase in the initial Ir(IV) concentration. The explanation is the same as for the saturation of Im-C_{11}-SH SAMs described above. The uncertainties, which are primarily determined by the counting precision, are reported at the 1σ (68% confidence level).

Table 5. The measured concentration of Ir(IV) solutions in 0.55 M HCl before and after sorption, and comparison of the surface saturation of MDDA-functionalized Au-coated glass chips with Ir(IV). The uncertainties are at the 1σ (68% confidence level).

	Substrate	
	MDDA SAMs on precleaned Au-coated glass chips	
$C_{\text{Ir init}}$ ($\cdot 10^{-8}$ M)	51.71 ± 0.26	543.1 ± 3.2
$C_{\text{Ir eq}}$ ($\cdot 10^{-8}$ M)	51.56 ± 0.21	522.1 ± 2.2
V_{Ir} ($\cdot 10^{-3}$ L)	3	3
ΔN_{Ir} ($\cdot 10^{14}$ molecules)	<0.09	3.8 ± 0.7
N_{MDDA} ($\cdot 10^{14}$ molecules/cm^2) [9]	4.5	
SS (%)	<2.0	84 ± 16

the quantities provided in this table are defined in the main text.

4. Conclusions

In this work, the surface characterization of Au-coated chips functionalized with Im-C_{11}-SH and MDDA SAMs was performed. AFM revealed that the SAMs deposition, as well as the liquid-UVPO treatment, do not affect the surface morphology and topology. The surface roughness values remain in the order of 1.20-1.25 nm. NP-SIMs showed that the highest surface coverage of (99 ± 6)% was reached when the SAMs deposition was performed twice from a 5 mM Im-C_{11}-SH solution. Precleaning of Au-coated silicon chips using the liquid-UVPO treatment enabled the use of surfaces free of numerous contaminants. The XPS stability study of Im-C_{11}-SH and MDDA SAMs under ambient laboratory conditions indicated that the functionalized

Au-coated chips remain stable for at least one month of their storage in closed wafer carrier trays when wrapped with aluminum foil. This makes it possible to use Im-C_{11}-SH and MDDA SAMs for the functionalization of Au-coated silicon detectors utilized during long-duration online cyclotron-based experiments. Also, the liquid-UVPO treatment was found to be an effective technique to regenerate the Au surfaces covered with Im-C_{11}-SH SAMs. Finally, ellipsometry results showed the presence of a single thiolate monolayer with a thickness of 1.690 ± 0.014 nm on the surface of Au. After one week of sample storage, the thickness remained relatively the same and excludes significant degradation processes during this period. NP-SIMS and INAA illustrated the successful sorption of Rh(III) and Ir(IV), respectively, on precleaned functionalized Au-coated chips. The coverage of Im-C_{11}-SH SAMs with Rh(III) was measured to be (81.3 ± 3.8)% using NP-SIMS. INAA results led to the conclusion that Ir(IV) can be adsorbed on Au-coated silicon chips functionalized with Im-C_{11}-SH SAMs with a surface saturation of (77 ± 12)% from a

5.4 μM initial Ir(IV) solution in 0.55 M HCl. The surface saturation of MDDA SAMs with Ir(IV) was measured to be (84 ± 16)% from a 5.4 μM initial Ir(IV) solution in 0.55 M HCl.

5. Declaration of competing interest

There are no competing interests to declare.

6. Acknowledgements

This material is based upon work supported by the U.S. Department of Energy, Office of Science, Office of Nuclear Physics under Award Number DE-FG02-93ER40773. The authors acknowledge the AFM and the XPS measurements were performed in the Texas A&M University Materials Characterization Core Facility (RRID:SCR_022202). The authors wish to thank

Dr. W. Serem for performing the AFM measurements, providing training, and assisting with interpreting data, as well as Dr. J. Wu for performing the XPS measurements and assisting with interpreting data. The authors thank Dr. S.V. Verkhoturov and Dr. D.S. Verkhoturov for performing the NP-SIMS measurements at the Department of Chemistry, Texas A&M University, and for assisting with interpreting data. The authors would like to thank Dr. B.E. Tomlin for conducting the INAA measurements at TEES Nuclear Science Center 1 MW TRIGA reactor. The authors would like to thank the Department of Biomedical Engineering, Texas A&M University, for providing access to the ellipsometer.

7. References

[1] R. Eichler *et al.*, Thermochemical and physical properties of element 112, Angew. Chem. Int. Ed. 47 (2008) 3262–3266, https://doi.org/10.1002/anie.200705019.

[2] R. Eichler *et al.*, Chemical characterization of element 112, Nature 447 (2007) 72–75, https://doi.org/10.1038/nature05761.

[3] A. Yakushev *et al.*, First study on nihonium (Nh, element 113) chemistry at TASCA, Front. Chem. 9 (2021) 1–9, https://doi.org/10.3389/fchem.2021.753738.

[4] S. N. Dmitriev *et al.*, Pioneering experiments on the chemical properties of element 113, Mendeleev Commun. 24 (2014) 253–256, https://doi.org/10.1016/j.mencom.2014.09.001.

[5] E. E. Tereshatov, M. Y. Boltoeva, D. Krupp, C. Baley, U. W. Scherer, and C. M. Folden III, *Surface functionalization with ionic liquids*, Cyclotron Institute, Texas A&M University (2017-2018, unpublished), available at https://cyclotron.tamu.edu/progress-reports/2017-2018/2%20Heavy%20Ion%20Reactions/II_34_35_Surface%20functionalization%20with%20ionic%20liquids.pdf.

[6] D. Krupp and U. W. Scherer, Prototype development of ion exchanging alpha detectors, Nucl. Instrum. Methods Phys. Res. A: Accel. Spectrom. Detect. Assoc. Equip. 897 (2018) 120–128, https://doi.org/10.1016/j.nima.2018.04.038.

[7] C. Vericat, M. E. Vela, G. Corthey, E. Pensa, E. Cortés, M. H. Fonticelli, F. Ibañez, G. E. Benitez, P. Carro, and R. C. Salvarezza, Self-assembled monolayers of thiolates on metals: A review article on sulfur-metal chemistry and surface structures, RSC Adv. 4 (2014) 27730–27754, https://doi.org/10.1039/C4RA04659E.

[8] C. Vericat, M. E. Vela, G. Benitez, P. Carro, and R. C. Salvarezza, Self-assembled monolayers of thiols and dithiols on gold: New challenges for a well-known system, Chem. Soc. Rev. 39 (2010) 1805–1834, https://doi.org/10.1039/B907301A.

[9] J. C. Love, L. A. Estroff, J. K. Kriebel, R. G. Nuzzo, and G. M. Whitesides, Self-assembled monolayers of thiolates on metals as a form of nanotechnology, Chem. Rev. 105 (2005) 1103–1170, https://doi.org/10.1021/cr0300789.

[10] J. L. Wilbur and G. M. Whitesides, in *Nanotechnology*, edited by G. Timp (Springer-Verlag, New York, NY, 1999), https://doi.org/10.1007/978-1-4612-0531-9

[11] A. Ulman, Formation and structure of self-assembled monolayers, Chem. Rev. 96 (1996) 1533–1554, https://doi.org/10.1021/cr9502357.

[12] J. Telegdi, Formation of self-assembled anticorrosion films on different metals, Materials 13 (2020) https://doi.org/10.3390/ma13225089.

[13] J. A. Woollam Co. Inc., in *CompleteEASE™ data analysis manual* (2011),

[14] C. D. Bain, E. B. Troughton, Y. T. Tao, J. Evall, G. M. Whitesides, and R. G. Nuzzo, Formation of monolayer films by the spontaneous assembly of organic thiols from solution onto gold, J. Am. Chem. Soc. 111 (1989) 321–335, https://doi.org/10.1021/ja00183a049.

[15] D. A. Offord, S. B. Sachs, M. S. Ennis, T. A. Eberspacher, J. H. Griffin, C. E. D. Chidsey, and J. P. Collman, Synthesis and properties of metalloporphyrin monolayers and stacked multilayers bound to an electrode via site specific axial ligation to a self-assembled monolayer, J. Am. Chem. Soc. 120 (1998) 4478–4487, https://doi.org/10.1021/ja973528l.

[16] M. Prato, R. Moroni, F. Bisio, R. Rolandi, L. Mattera, O. Cavalleri, and M. Canepa, Optical characterization of thiolate self-assembled monolayers on Au(111), J. Phys. Chem. C 112 (2008) 3899–3906, https://doi.org/10.1021/jp711194s.

[17] L. Qi, H. Tian, and H.-Z. Yu, Binary thiolate DNA/ferrocenyl self-assembled monolayers on gold: A versatile platform for probing biosensing interfaces, Anal. Chem. 90 (2018) 9174–9181, https://doi.org/10.1021/acs.analchem.8b01655.

[18] T. Ito, H. Coceancigh, Y. Yi, J. N. Sharma, F. C. Parks, and A. H. Flood, Nanoporous thin films formed from photocleavable diblock copolymers on gold substrates modified with thiolate self-assembled monolayers, Langmuir 36 (2020) 9259–9268, https://doi.org/10.1021/acs.langmuir.0c01572.

[19] S. Brown, J. D. Sayler, and S. J. Sibener, Influence of structural dynamics on the kinetics of atomic hydrogen reactivity with low-temperature alkanethiolate self-assembled monolayers, J. Phys. Chem. C 125 (2021) 24406–24412, https://doi.org/10.1021/acs.jpcc.1c07487.

[20] A. Asyuda, S. Das, and M. Zharnikov, Thermal stability of alkanethiolate and aromatic thiolate self-assembled monolayers on Au(111): An X-ray photoelectron spectroscopy study, J. Phys. Chem. C 125 (2021) 21754–21763, https://doi.org/10.1021/acs.jpcc.1c06984.

[21] R. Urcuyo, E. Cortés, A. A. Rubert, G. Benitez, M. L. Montero, N. G. Tognalli, A. Fainstein, M. E. Vela, and R. C. Salvarezza, Aromatic and aliphatic thiol self-assembled monolayers on Au: Anchoring and delivering copper species, J. Phys. Chem. C 115 (2011) 24707–24717, https://doi.org/10.1021/jp207875g.

[22] L. V. Protsailo, W. R. Fawcett, D. Russell, and R. L. Meyer, Electrochemical characterization of the alkaneselenol-based sams on Au(111) single crystal electrode, Langmuir 18 (2002) 9342–9349, https://doi.org/10.1021/la0203483.

[23] J. Ossowski *et al.*, Thiolate versus selenolate: Structure, stability, and charge transfer properties, ACS Nano 9 (2015) 4508–4526, https://doi.org/10.1021/acsnano.5b01109.

[24] J. Ossowski, J. Rysz, A. Terfort, and P. Cyganik, Relative stability of thiolate and selenolate sams on Ag(111) substrate studied by static sims. Oscillation in stability of consecutive chemical bonds, J. Phys. Chem. C 121 (2017) 459–470, https://doi.org/10.1021/acs.jpcc.6b10762.

[25] T. M. Owens, B. J. Ludwig, D. R. Fosnacht, J. M. Bartolin, N. Homann, N. J. Wells, B. G. Orr, and M. M. Banaszak Holl, Octylgermane on gold: Synthesis, oxidation, and pattern formation, Langmuir 20 (2004) 11422–11427, https://doi.org/10.1021/la0490846.

[26] S.-H. Song, P. Koelsch, T. Weidner, M. S. Wagner, and D. G. Castner, Sodium dodecyl sulfate adsorption onto positively charged surfaces: Monolayer formation with opposing headgroup orientations, Langmuir 29 (2013) 12710–12719, https://doi.org/10.1021/la401119p.

[27] Z. Wang, J. Chen, S. Oyola-Reynoso, and M. Thuo, Empirical evidence for roughness-dependent limit in observation of odd–even effect in wetting properties of polar liquids on n-alkanethiolate self-assembled monolayers, Langmuir 32 (2016) 8230–8237, https://doi.org/10.1021/acs.langmuir.6b02159.

[28] S. W. Han, S. J. Lee, and K. Kim, Self-assembled monolayers of aromatic thiol and selenol on silver: Comparative study of adsorptivity and stability, Langmuir 17 (2001) 6981–6987, https://doi.org/10.1021/la010464q.

[29] J. Rechmann, M. Krzywiecki, and A. Erbe, Carbon–sulfur bond cleavage during adsorption of octadecane thiol to copper in ethanol, Langmuir 35 (2019) 6888–6897, https://doi.org/10.1021/acs.langmuir.9b00686.

[30] D.-Q. Zhang, X.-M. He, Q.-R. Cai, L.-X. Gao, and G. S. Kim, pH and iodide ion effect on corrosion inhibition of histidine self-assembled monolayer on copper, Thin Solid Films 518 (2010) 2745–2749, https://doi.org/10.1016/j.tsf.2009.10.150.

[31] Y. Qiang, H. Li, and X. Lan, Self-assembling anchored film basing on two tetrazole derivatives for application to protect copper in sulfuric acid environment, J. Mater. Sci. Technol. 52 (2020) 63–71, https://doi.org/10.1016/j.jmst.2020.04.005.

[32] G. Kumar, C.-H. Lien, M. J. Janik, and J. W. Medlin, Catalyst site selection via control over noncovalent interactions in self-assembled monolayers, ACS Catal. 6 (2016) 5086–5094, https://doi.org/10.1021/acscatal.6b01074.

[33] H. Solodenko, P. Stender, and G. Schmitz, Atom probe study of 1-octadecanethiol self-assembled monolayers on platinum (111) and (200) surfaces, Microsc. Microanal. (2021) 1–10, https://doi.org/10.1017/S1431927621012654.

[34] K. Senthil kumar, L. Jiang, and C. A. Nijhuis, Fabrication of ultra-smooth and oxide-free molecule-ferromagnetic metal interfaces for applications in molecular electronics under ordinary laboratory conditions, RSC Adv. 7 (2017) 14544–14551, https://doi.org/10.1039/C6RA27280K.

[35] G. Mani, D. M. Johnson, D. Marton, V. L. Dougherty, M. D. Feldman, D. Patel, A. A. Ayon, and C. M. Agrawal, Stability of self-assembled monolayers on titanium and gold, Langmuir 24 (2008) 6774–6784, https://doi.org/10.1021/la8003646.

[36] Y. Feng, S. Chen, J. You, and W. Guo, Investigation of alkylamine self-assembled films on iron electrodes by SEM, FT-IR, EIS and molecular simulations, Electrochim. Acta 53 (2007) 1743–1753, https://doi.org/10.1016/j.electacta.2007.08.035.

[37] Y. Paz, Self-assembled monolayers and titanium dioxide: From surface patterning to potential applications, Beilstein J. Nanotechnol. 2 (2011) 845–861, https://doi.org/10.3762/bjnano.2.94.

[38] A. Raman, R. Quiñones, L. Barriger, R. Eastman, A. Parsi, and E. S. Gawalt, Understanding organic film behavior on alloy and metal oxides, Langmuir 26 (2010) 1747–1754, https://doi.org/10.1021/la904120s.

[39] C. E. Taylor and D. K. Schwartz, Octadecanoic acid self-assembled monolayer growth at sapphire surfaces, Langmuir 19 (2003) 2665–2672, https://doi.org/10.1021/la026218b.

[40] G. A. Somorjai and Y. Li, *Introduction to surface chemistry and catalysis*, 2nd ed., (Wiley, Hoboken, NJ, 2010).

[41] K. W. Kolasinski, *Surface science: Foundations of catalysis and nanoscience*, 4th ed., (Wiley, Hoboken, NJ, USA, 2020).

[42] H. S. Kato, S. Yoshimoto, A. Ueda, S. Yamamoto, Y. Kanematsu, M. Tachikawa, H. Mori, J. Yoshinobu, and I. Matsuda, Strong hydrogen bonds at the interface between proton-donating and -accepting self-assembled monolayers on Au(111), Langmuir 34 (2018) 2189–2197, https://doi.org/10.1021/acs.langmuir.7b03451.

[43] J. Wei, H. Liu, A. R. Dick, H. Yamamoto, Y. He, and D. H. Waldeck, Direct wiring of cytochrome c's heme unit to an electrode: Electrochemical studies, J. Am. Chem. Soc. 124 (2002) 9591-9599, https://doi.org/10.1021/ja025518c.

[44] A. J. Zaitouna and R. Y. Lai, Design and characterization of a metal ion–imidazole self-assembled monolayer for reversible immobilization of histidine-tagged peptides, Chem. Commun. 47 (2011) 12391–12393, https://doi.org/10.1039/C1CC15510E.

[45] L. Tian, X. Song, X. Yu, and W. Hu, Modulated rectification of carboxylate-terminated self-assembled monolayer junction by humidity and alkali metal ions: The coupling and asymmetric factor matter, J. Phys. Chem. C 125 (2021) 21614-21623, https://doi.org/10.1021/acs.jpcc.1c05259.

[46] C. Magallanes, B. M. Aguirre, G. A. González, and L. P. Méndez De Leo, Interaction of aqueous Cu(II) with carboxylic acid and alcohol terminated self assembled monolayers: Surface and interfacial characterization, Surf. Sci. 692 (2020) 121529, https://doi.org/10.1016/j.susc.2019.121529.

[47] L. Tian, A. Fan, X. Yu, and W. Hu, Achieving high-performance molecular rectification through fast screening alkanethiol carboxylate-metal complexes electroactive units, CCS Chemistry 5 (2023) 902-914, https://doi.org/10.31635/ccschem.022.202201890.

[48] V. Ivanova, M. Manolova, and D. Kolb, Palladium and platinum deposition onto 4-mercaptopyridine SAMs, Solid State Phenom. 121-123 (2007) 363–368, https://doi.org/10.4028/www.scientific.net/SSP.121-123.363.

[49] J. Kochana, K. Starzec, M. Wieczorek, P. Knihnicki, M. Góra, A. Rokicińska, P. Kościelniak, and P. Kuśtrowski, Study on self-assembled monolayer of functionalized thiol on gold electrode forming capacitive sensor for chromium(VI) determination, J. Solid State Electrochem. 23 (2019) 1463–1472, https://doi.org/10.1007/s10008-019-04236-2.

[50] Y. Li, S. E. Root, L. Belding, J. Park, J. Rawson, H. J. Yoon, M. Baghbanzadeh, P. Rothemund, and G. M. Whitesides, Characterizing chelation at surfaces by charge tunneling, J. Am. Chem. Soc. 143 (2021) 5967-5977, https://doi.org/10.1021/jacs.1c01800.

[51] J. Park, L. Belding, L. Yuan, M. P. S. Mousavi, S. E. Root, H. J. Yoon, and G. M. Whitesides, Rectification in molecular tunneling junctions based on alkanethiolates with bipyridine–metal complexes, J. Am. Chem. Soc. 143 (2021) 2156-2163, https://doi.org/10.1021/jacs.0c12641.

[52] H. J. Yoon, K.-C. Liao, M. R. Lockett, S. W. Kwok, M. Baghbanzadeh, and G. M. Whitesides, Rectification in tunneling junctions: 2,2′-bipyridyl-terminated n-alkanethiolates, J. Am. Chem. Soc. 136 (2014) 17155-17162, https://doi.org/10.1021/ja509110a.

[53] H. Kang, S. J. Cho, G. D. Kong, and H. J. Yoon, Li-ion intercalation, rectification, and solid electrolyte interphase in molecular tunnel junctions, Nano Letters 22 (2022) 4956-4962, https://doi.org/10.1021/acs.nanolett.2c01669.

[54] R. K. Shervedani, A. Farahbakhsh, and M. Bagherzadeh, Functionalization of gold cysteamine self-assembled monolayer with ethylenediaminetetraacetic acid as a novel nanosensor, Analytica Chimica Acta 587 (2007) 254-262, https://doi.org/10.1016/j.aca.2007.01.053.

[55] C.-H. K. Wang, S. Jiang, and S. H. Pun, Localized cell uptake of his-tagged polyplexes immobilized on NTA self-assembled monolayers, Langmuir 26 (2010) 15445-15452, https://doi.org/10.1021/la1025203.

[56] N. Papaiconomou, I. Billardde, and E. Chaine, Extraction of iridium(IV) from aqueous solutions using hydrophilic/hydrophobic ionic liquids, RSC Adv. 4 (2014) 48260–48266, https://doi.org/10.1039/c4ra06991a.

[57] Y. Yan, Q. Wang, Z. Xiang, and Y. Yang, Separation of Pt(IV), Pd(II), Ru(III), and Rh(III) from chloride medium using liquid–liquid extraction with mixed imidazolium-based ionic liquids, Sep. Sci. Technol. 53 (2018) 2064–2073, https://doi.org/10.1080/01496395.2018.1440304.

[58] S. Yamamoto *et al.*, Direct evidence of interfacial hydrogen bonding in proton-electron concerted 2D organic bilayer on au substrate, e-J. Surf. Sci. Nanotechnol. 17 (2019) 49–55, https://doi.org/10.1380/ejssnt.2019.49.

[59] V. Zakusilova, E. E. Tereshatov, M. Boltoeva, and C. M. Folden III, *Metal adsorption on functionalized silicon detectors for the future study of meitnerium chemistry*, in Progress in Research, Cyclotron Institute, Texas A&M University (2021-2022), pp. II-28–II-31, available at https://cyclotron.tamu.edu/progress-reports/2021-2022/cyclotron_progress_2022.pdf.

[60] V. Zakusilova, Doctor of Philosophy Thesis, University of Strasbourg (2022), available at http://www.theses.fr/2022STRAE020/document.

[61] V. Zakusilova, E. E. Tereshatov, K. L. Childers, J. A. Mildon, J. R. Garcia, I. W. Haynes, S. M. Loftin, and C. M. Folden III, Element sorption on thiolate-functionalized gold-coated silicon detectors in the isothermal online gas-phase experiments, in preparation

[62] B. N. Johnson and R. Mutharasan, Regeneration of gold surfaces covered by adsorbed thiols and proteins using liquid-phase hydrogen peroxide-mediated UV-photooxidation, J. Phys. Chem. C 117 (2013) 1335–1341, https://doi.org/10.1021/jp307983e.

[63] MilliporeSigma, *1-(11-mercaptoundecyl)imidazole,* 723088, available at https://www.sigmaaldrich.com/US/en/product/aldrich/723088.

[64] MilliporeSigma, *12-mercaptododecanoic acid,* 675067, available at https://www.sigmaaldrich.com/US/en/product/aldrich/675067?gclid=CjwKCAjwlqOXBhBqEiwA-hhitPEthpnY5KuVC6gh4vfT8I6OFWR2QMja2e6Jq8nR8yQP95HXD5s5choCZAMQAvD_BwE.

[65] L. Houssiau and P. Bertrand, TOF–SIMS study of alkanethiol adsorption and ordering on gold, Appl. Surf. Sci. 175–176 (2001) 399–406, https://doi.org/10.1016/S0169-4332(01)00132-5.

[66] T. L. Barr and S. Seal, Nature of the use of adventitious carbon as a binding energy standard, J. Vac. Sci. Technol. A 13 (1995) 1239–1246, https://doi.org/10.1116/1.579868.

[67] F. Mangolini, J. B. McClimon, F. Rose, and R. W. Carpick, Accounting for nanometer-thick adventitious carbon contamination in X-ray absorption spectra of carbon-based materials, Anal. Chem. 86 (2014) 12258–12265, https://doi.org/10.1021/ac503409c.

[68] M. J. Eller, Doctor of Philosophy Thesis, Texas A&M University (2012), available at https://hdl.handle.net/1969.1/148366.

[69] C.-K. Liang, Doctor of Philosophy Thesis, Texas A&M University (2014), available at https://hdl.handle.net/1969.1/153571.

[70] C.-K. Liang, S. Verkhoturov, and L.-J. Chen, Size-dependent emission of negative ions from gold nanoparticles bombarded with C_{60} and Au_{400}, Int. J. Mass Spectrom. 334 (2013) 43–48, https://doi.org/10.1016/j.ijms.2012.10.003.

[71] M. A. Park, K. A. Gibson, K. Quinones, and M. A. Schweikert, Coincidence counting in time-of-flight mass spectrometry: A test for chemical microhomogeneity, Science 248 (1990) 988–990, https://doi.org/10.1126/science.248.4958.988.

[72] D. S. Verkhoturov, B. P. Crulhas, M. J. Eller, Y. D. Han, S. V. Verkhoturov, Y. Bisrat, A. Revzin, and E. A. Schweikert, Nanoprojectile secondary ion mass spectrometry for analysis of extracellular vesicles, Anal. Chem. 93 (2021) 7481–7490, https://doi.org/10.1021/acs.analchem.1c00689.

[73] M. J. Eller, J. M. Sandoval, S. V. Verkhoturov, and E. A. Schweikert, Nanoprojectile secondary ion mass spectrometry for nanometrology of nanoparticles and their interfaces, Anal. Chem. 94 (2022) 7868–7876, https://doi.org/10.1021/acs.analchem.2c00303.

[74] E. A. Weiss, R. C. Chiechi, G. K. Kaufman, J. K. Kriebel, Z. Li, M. Duati, M. A. Rampi, and G. M. Whitesides, Influence of defects on the electrical characteristics of mercury-drop junctions: Self-assembled monolayers of n-alkanethiolates on rough and smooth silver, J. Am. Chem. Soc. 129 (2007) 4336-4349, https://doi.org/10.1021/ja0677261.

[75] E. A. Weiss, G. K. Kaufman, J. K. Kriebel, Z. Li, R. Schalek, and G. M. Whitesides, Si/SiO_2-templated formation of ultraflat metal surfaces on glass, polymer, and solder supports: Their use as substrates for self-assembled monolayers, Langmuir 23 (2007) 9686-9694, https://doi.org/10.1021/la701919r.

[76] T. M. Willey, A. L. Vance, T. van Buuren, C. Bostedt, L. J. Terminello, and C. S. Fadley, Rapid degradation of alkanethiol-based self-assembled monolayers on gold in ambient laboratory conditions, Surf. Sci. 576 (2005) 188–196, https://doi.org/10.1016/j.susc.2004.12.022.

[77] M. Zharnikov and M. Grunze, Modification of thiol-derived self-assembling monolayers by electron and X-ray irradiation: Scientific and lithographic aspects, J. Vac. Sci. Technol. B 20 (2002) 1793–1807, https://doi.org/10.1116/1.1514665.

[78] *XPS reference table of elements*, retrieved 19 April 2022, available at https://www.jp.xpssimplified.com/elements/sulfur.php.

[79] V. Feyer, O. Plekan, S. Ptasińska, M. Iakhnenko, N. Tsud, and K. C. Prince, Adsorption of histidine and a histidine tripeptide on Au(111) and Au(110) from acidic solution, J. Phys. Chem. C 116 (2012) 22960-22966, https://doi.org/10.1021/jp307463z.

[80] Z. Safaei, A. Shiroudi, E. Zahedi, and M. Sillanpää, Atmospheric oxidation reactions of imidazole initiated by hydroxyl radicals: Kinetics and mechanism of reactions and atmospheric implications, Phys. Chem. Chem. Phys. 21 (2019) 8445–8456, https://doi.org/10.1039/C9CP00632J.

[81] E. Cortés, A. A. Rubert, G. Benitez, P. Carro, M. E. Vela, and R. C. Salvarezza, Enhanced stability of thiolate self-assembled monolayers (SAMs) on nanostructured gold substrates, Langmuir 25 (2009) 5661–5666, https://doi.org/10.1021/la804251a.

[82] G. Yang, N. A. Amro, Z. B. Starkewolfe, and G. Y. Liu, Molecular-level approach to inhibit degradations of alkanethiol self-assembled monolayers in aqueous media, Langmuir 20 (2004) 3995–4003, https://doi.org/10.1021/la0499160.

[83] R. K. Gupta, M. P. Srinivasan, and R. Dharmarajan, Synthesis of 16-mercaptohexadecanoic acid capped gold nanoparticles and their immobilization on a substrate, Mater. Lett. 67 (2012) 315–319, https://doi.org/10.1016/j.matlet.2011.09.047.

[84] *Ellipsometry tutorial*, retrieved 4 March 2021, available at https://www.jawoollam.com/resources/ellipsometry-tutorial.

[85] M. J. Eller, S. V. Verkhoturov, and E. A. Schweikert, Testing molecular homogeneity at the nanoscale with massive cluster secondary ion mass spectrometry, Anal. Chem. 88 (2016) 7639–7646, https://doi.org/10.1021/acs.analchem.6b01466.

[86] V. Zakusilova, G. Zante, E. E. Tereshatov, C. M. Folden III, and M. Boltoeva, Extraction and separation of iridium(IV) and rhodium(III) from hydrochloric acid media by a quaternary ammonium-based hydrophobic eutectic solvent, Sep. Purif. Technol. 278 (2021) 118814, https://doi.org/10.1016/j.seppur.2021.118814.

[87] M. N. Le, M. S. Lee, and G. Senanayake, A short review of the separation of iridium and rhodium from hydrochloric acid solutions by solvent extraction, J. Solution Chem. 47 (2018) 1373–1394, https://doi.org/10.1007/s10953-018-0770-8.

[88] S. F. Mughabghab, Thermal neutron capture cross sections resonance integrals and g-factors (2003), available at https://www.osti.gov/etdeweb/servlets/purl/20332542.

[89] J. Blachot, Nuclear data sheets for A = 104, Nucl. Data Sheets 108 (2007) 2035–2172, https://doi.org/10.1016/j.nds.2007.09.001.

[90] C. M. Baglin, Nuclear data sheets for A = 192, Nucl. Data Sheets 113 (2012) 1871–2111, https://doi.org/10.1016/j.nds.2012.08.001.

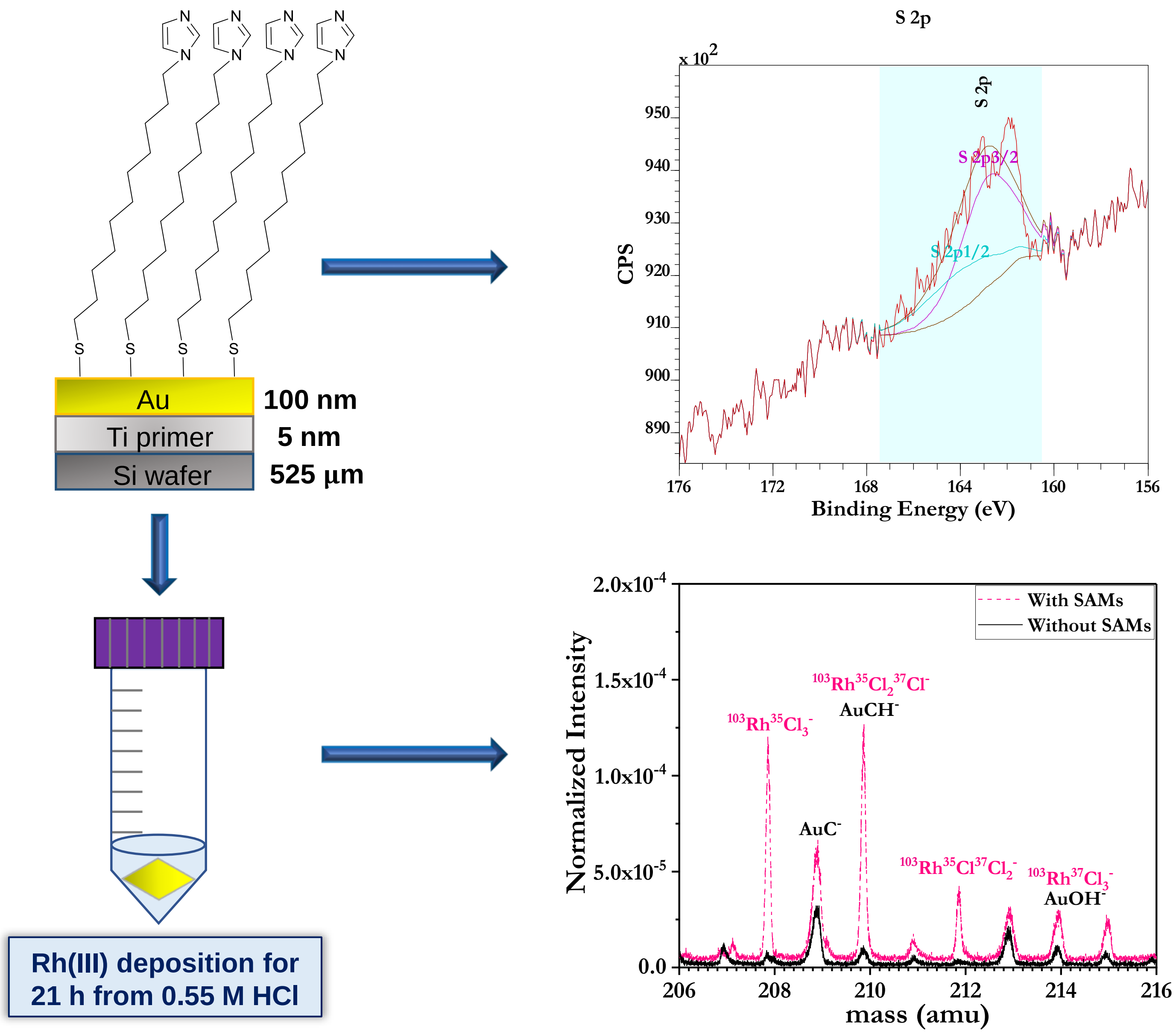

Au
Ti primer
Si wafer
100 nm
5 nm
525 µm
Rh(III) deposition for
21 h from 0.55 M HCl
S 2p
x 10^2
CPS
Binding Energy (eV)
S 2p3/2
S 2p1/2
Normalized Intensity
mass (amu)
With SAMs
Without SAMs
103Rh35Cl3-
103Rh35Cl237Cl-
AuCH-
AuC-
103Rh35Cl37Cl2-
103Rh37Cl3-
AuOH-